CHAPTER 7 – MODELS AND INSPECTION PROCEDURE FOR A CYLINDRICAL HOLE WITH AN ELASTIC INSERT

7.1 Background

The Air Force is currently sponsoring the development of an ultrasonic technique for the detection of fatigue cracks in holes containing fasteners. Two field examples are the C-141 rib clip holes and the C-130 beam cap holes. These hole cases contain fasteners made of aluminum or sometimes steel. These two inspection configurations are similar to the C-141 weep hole case in that they are located within a riser with access limited for an ultrasonic transducer to a single surface. As for the weep hole case, the feasibility of ultrasonic inspection using 'leaky' Rayleigh waves generated about the cylindrical hole was investigated.

Considerable prior work has studied the ultrasonic scattering from cylindrical inclusions perfectly bonded to an infinite elastic media [74,52,62,75,67]. These works have not directly examined interface waves between the inclusion and the elastic medium. For the case of two elastic half-spaces with similar material properties that have welded contact at the interface, the generated interface waves between the two materials are typically insignificant in magnitude [61]. Given this result, the application of the 'leaky' Rayleigh wave inspection technique for holes with elastic inserts in welded

contact seems unlikely. However for the case of smooth contact between two elastic half-spaces of similar material properties, significant interface waves do exist [61]. Thus for the smooth contact case, the initial indication for inspection using the 'leaky' Rayleigh wave technique is promising.

The real interface condition probably lies between these two ideal conditions: welded and smooth contact. The C-141 rib clip hole and the C-130 beam cap hole contain fasteners that are loosely fit in the hole. On occasion, a fluid layer may exist between the hole surface and the insert. The transmission of little to no shear traction at the interface is thus expected. A review of the ultrasonic assessment of imperfect interfaces was performed by Nagy [76]. The interface for these inspection cases can be classified as a slip bond [76].

A variety of interface conditions can be modeled using the finite interfacial stiffnesses [76]. A relation can be defined where the change in displacement across the interface is proportional to the traction components. Written in terms of normal and tangential components, the relationships are given by

$$t_n^A = s_n^A = K_n\left[u_n - v_n\right] \tag{7.1}$$

$$t_t^A = s_t^A = K_t\left[u_t - v_t\right] \tag{7.2}$$

The ratio of the K_t/K_n can be used to characterize the nature of the bond. For water, this ratio can be as low as 1.5E–10 for 5.0 MHz waves [76]. This indicates that the interface condition for our case may be approximated as a 'smooth' boundary condition, where no shear tractions are transmitted across the interface. Prior work examining the ultrasonic

scattering from an elastic interface between a cylindrical insert and an elastic medium has primarily addressed composite material applications. Huang and Rokhlin have examined through an analytic approach the scattering of elastic cylinders embedded in infinite elastic matrices with stiffness interfaces for incident longitudinal plane waves [77].

To model the ultrasonic inspection of notches on a cylindrical cavity with an elastic insert and a stiffness interface, advanced models are required. In this Dissertation, a BEM model was developed to study this case. With this model, the nature of the waves propagating about the interface and scattering from a surface breaking notch was explored. Using the simulated and experimental results, an ultrasonic inspection technique was developed. Lastly, an understanding of the sensitivity of the inspection technique to variation in measurement, geometric and material parameters was explored.

7.2 Analytic Model Development

To develop an initial understanding of the scattering phenomenon and to have a means for validating the BEM simulation, an analytic model for the scattering of an incident plane shear wave by an elastic insert in a cylindrical hole was developed. Figure 7.1 displays a diagram of the configuration. The analytic solution for scattering of a plane wave incident on a cylindrical hole containing an elastic insert was previously derived [74,52]. The incident transient signal and the corresponding frequency spectrum

representing a typical transducer transient signal used for this study is given in Figures 7.2(a) and 7.2(b) respectively. The solution to the significant frequency components was solved and Fourier transforms were used to reconstruct the transient response. A transient pulse with a broader bandwidth was chosen for increased spatial resolution of the transient signals. This analysis approach was also used by Nagy et al to investigate the fluid-filled hole case [20].

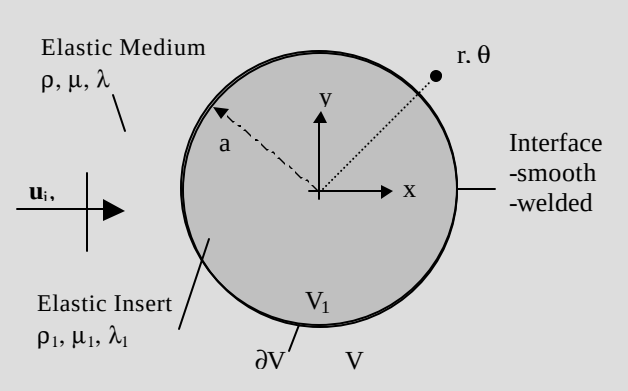

Figure 7.1. Cylindrical hole in an infinite elastic media containing an elastic insert.

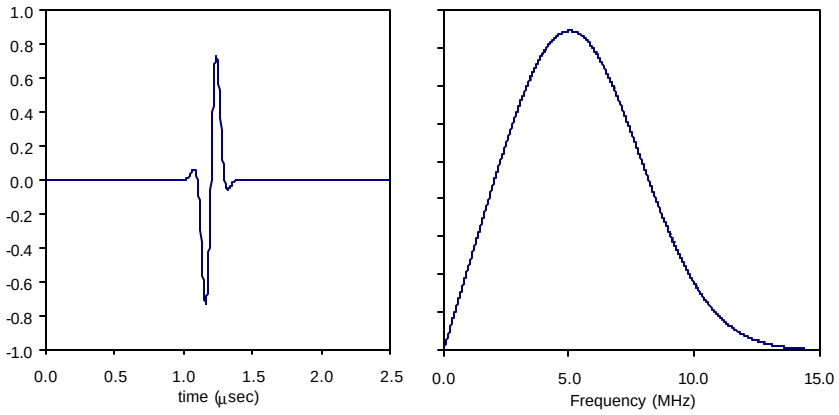

Figure 7.2. Transient broadband pulse (a) in time domain, and (b) frequency spectrum.

7.3 BEM Model Development

In order to simulate the response of an incident transducer signal by a cavity in an infinite elastic medium containing an elastic insert and a stiffness interface, the boundary element method was used. Simulations for the no-notch and with-notch cases were developed. The configurations for these simulations are shown in Figure 7.3. Some prior studies have investigated the scattering from a cylindrical hole in an elastic medium containing an elastic inclusion using the boundary element method. Niwa et al examined the transient scattering response of a plane elastic wave by an elastic inclusion in an elastic half space using the frequency domain boundary integral equation method [25]. Our study will be an extension of this work.

The equation of motion for an elastic solid is given by

$$(l+m)\tilde{\nabla}\tilde{\nabla}\cdot\mathbf{u}(\mathbf{x},t)+m\nabla^2\mathbf{u}(\mathbf{x},t)=\rho\ddot{\mathbf{u}}(\mathbf{x},t) \tag{7.3}$$

The steady state form of the equation of motion in the transformed domain for an elastic solid is given by

$$(l+m)\tilde{\nabla}\tilde{\nabla}\cdot\hat{\mathbf{u}}(\mathbf{x},\omega)+m\nabla^2\hat{\mathbf{u}}(\mathbf{x},\omega)+\rho\omega^2\hat{\mathbf{u}}(\mathbf{x},\omega)=0 \tag{7.4}$$

To define traction conditions, Hooke's law and the strain relations are used. For an elastic insert in an infinite elastic media with a massless stiffness interface between the insert and the hole, the interface conditions are continuity of normal and shear traction where

$$\hat{t}_n(\mathbf{x},\omega)=\hat{s}_n(\mathbf{x},\omega),\ x\in\partial V, \tag{7.5}$$

$$\hat{t}_t(\mathbf{x},\boldsymbol{w}) = \hat{s}_t(\mathbf{x},\boldsymbol{w}),\ x \in \partial V\ . \tag{7.6}$$

The displacement discontinuity between the elastic solid and the elastic insert is governed by a stiffness interface condition for both the normal and tangential directions,

$$u_n(\mathbf{x},\boldsymbol{w}) = v_n(\mathbf{x},\boldsymbol{w}) + \frac{1}{K_n(\mathbf{x},\boldsymbol{w})} t_n(\mathbf{x},\boldsymbol{w}),\ x \in \partial V\ , \tag{7.7}$$

$$u_t(\mathbf{x},\boldsymbol{w}) = v_t(\mathbf{x},\boldsymbol{w}) + \frac{1}{K_t(\mathbf{x},\boldsymbol{w})} t_t(\mathbf{x},\boldsymbol{w}),\ x \in \partial V\ . \tag{7.8}$$

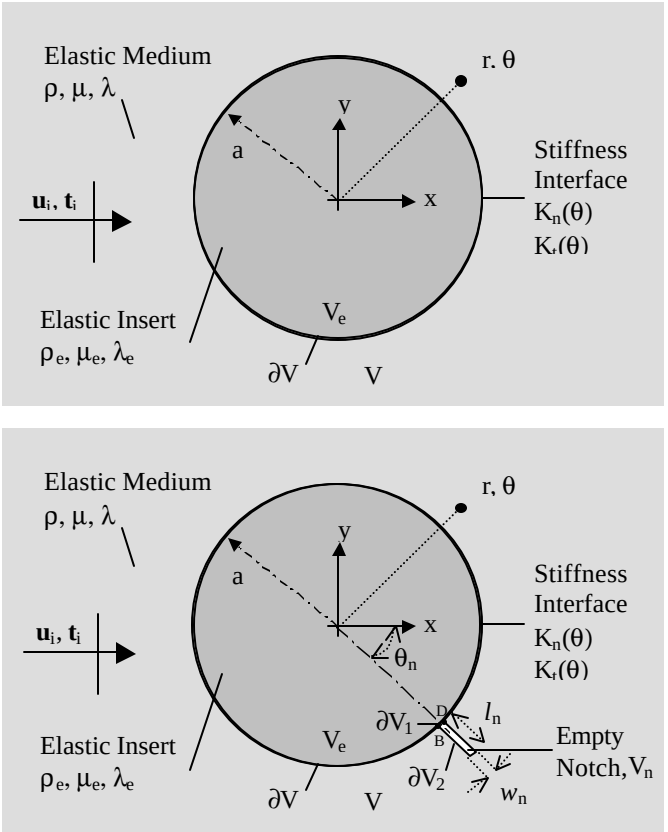

Figure 7.3. Cylindrical hole in an infinite elastic media containing an elastic insert with a stiffness interface for the (a) no-notch case and (b) with-notch case.

The variable **u** and **v** represent the displacements in the elastic medium and the insert respectively. The variables **t** and **s** represent the tractions in the elastic medium and the insert respectively. For the notch case, the notch is assumed to have a finite width with traction free boundary conditions. For the arc BD along the insert boundary at the notch mouth, the traction free boundary conditions are given by

$$\hat{s}_n(\mathbf{x},w) = 0\,,\ x \in \partial V_1\,, \tag{7.9}$$

$$\hat{s}_t(\mathbf{x},w) = 0\,,\ x \in \partial V_1\,. \tag{7.10}$$

For the notch boundary along the infinite elastic medium, the traction free boundary conditions are given by

$$\hat{t}_n(\mathbf{x},w) = 0\,,\ x \in \partial V_2\,, \tag{7.11}$$

$$\hat{t}_t(\mathbf{x},w) = 0\,,\ x \in \partial V_2\,. \tag{7.12}$$

Consider an arbitrary incident displacement field in the elastic medium, $\mathbf{u^i}$. The field scattered from the interface into the elastic medium will be defined as $\mathbf{u^{sc}}$. Thus the superposition of these two fields gives the total field response in the elastic medium, $\mathbf{u^t}$. The scattered response in the cylindrical elastic insert will be defined in terms of total displacement, $\mathbf{v^t}$. By substituting the displacements, $\mathbf{u^i} + \mathbf{u^{sc}}$, for $\mathbf{u^t}$, and the tractions, $\mathbf{t^i} + \mathbf{t^{sc}}$ for $\mathbf{t^t}$, the interface conditions become,

$$\hat{s}_n^{\,t}(\mathbf{x},w) = \hat{t}_n^{\,sc}(\mathbf{x},w) + \hat{t}_n^{\,i}(\mathbf{x},w)\,,\ x \in \partial V\,, \tag{7.13}$$

$$\hat{s}_t^{\,t}(\mathbf{x},w) = \hat{t}_t^{\,sc}(\mathbf{x},w) + \hat{t}_t^{\,i}(\mathbf{x},w)\,,\ x \in \partial V\,, \tag{7.14}$$

and continuity of displacement between the elastic solid and the elastic insert through a stiffness interface for both the normal and tangential directions where

$$v_n^{\,t}(\mathbf{x},w) = u_n^{\,sc}(\mathbf{x},w) + u_n^{\,i}(\mathbf{x},w) - \frac{1}{K_n(\mathbf{x},w)}\left[t_n^{\,sc}(\mathbf{x},w) + t_n^{\,i}(\mathbf{x},w)\right],\ x \in \partial V\,, \tag{7.15}$$

$$v_t^{\,t}(\mathbf{x},w) = u_t^{\,sc}(\mathbf{x},w) + u_t^{\,i}(\mathbf{x},w) - \frac{1}{K_t(\mathbf{x},w)}\left[t_t^{\,sc}(\mathbf{x},w) + t_t^{\,i}(\mathbf{x},w)\right],\ x \in \partial V\,. \tag{7.16}$$

Again, for the arc BD along the insert boundary at the notch mouth, the traction free boundary conditions are given by

$$\hat{s}_n^{\,t}(\mathbf{x},w) = 0\,,\ x \in \partial V_1\,, \tag{7.17}$$

$$\hat{s}_t^{\,t}(\mathbf{x},w) = 0\,,\ x \in \partial V_1\,. \tag{7.18}$$

Also, for the notch boundary with the infinite elastic medium, the traction free boundary conditions are given by

$$\hat{t}_n^{\,sc}(\mathbf{x},w) = -\hat{t}_n^{\,i}(\mathbf{x},w)\,,\ x \in \partial V_2\,, \tag{7.19}$$

$$\hat{t}_t^{\,sc}(\mathbf{x},w) = -\hat{t}_t^{\,i}(\mathbf{x},w)\,,\ x \in \partial V_2\,. \tag{7.20}$$

The integral equation for an infinite elastic domain and the elastic insert can be represented by

$$\int_{\partial V+\partial V_2}\left[\mathbf{U}(\mathbf{x},y;w)\hat{\mathbf{t}}^{sc}(y,w) - \mathbf{T}(\mathbf{x},y;w)\hat{\mathbf{u}}^{sc}(y,w)\right]\mathrm{dS}_y = \begin{matrix}\hat{\mathbf{u}}^{sc}(\mathbf{x};w), & \mathbf{x}\in \mathrm{V}\\ 0, & \mathbf{x}\in \mathrm{V_e}+\mathrm{V_n}\end{matrix} \tag{7.21}$$

and

$$\int_{\partial V-\partial V_1}\left[\mathbf{U}(\mathbf{x},y;w)\hat{\mathbf{s}}^{t}(y,w) - \mathbf{T}(\mathbf{x},y;w)\hat{\mathbf{v}}^{t}(y,w)\right]\mathrm{dS}_y = \begin{matrix}\hat{\mathbf{v}}^{t}(\mathbf{x};w), & \mathbf{x}\in \mathrm{V_e}\\ 0, & \mathbf{x}\in \mathrm{V}+\mathrm{V_n}\end{matrix}\,. \tag{7.22}$$

These integral equations are written for both the notch and no-notch cases. For the no-notch case, V_n and ∂V_1 and ∂V_2 equal zero. The fundamental solutions for the two dimensional problem, **U,** and the double layer kernal, **T,** are given in Section 2.2.

At this point, the boundaries are discretized into elements, and two separate systems of equations are derived for each of the integral equations. The results can be represented by the following matrix equations for the elastic solid and elastic insert respectively,

$$\mathbf{H}^{(1)}\hat{\mathbf{u}}^{sc} = \mathbf{G}^{(1)}\hat{\mathbf{t}}^{sc}, \tag{7.23}$$

$$\mathbf{H}^{(2)}\hat{\mathbf{v}}^{t} = \mathbf{G}^{(2)}\hat{\mathbf{s}}^{t}. \tag{7.24}$$

With the application of the interface conditions for the no-notch case (7.13-16) and for the notch case (7.13-20) and substitution of the incident displacement and traction field, a single system of equations can be written in the following form for the no-notch case

$$[\mathbf{A}]\begin{pmatrix}\hat{\mathbf{u}}^{sc}(x\in\partial V)\\ \hat{\mathbf{t}}^{sc}(x\in\partial V)\end{pmatrix}=\{\mathbf{B}\}, \tag{7.25}$$

and for the notch case

$$[\mathbf{A}']\begin{pmatrix}\hat{\mathbf{u}}^{sc}(x\in\partial V+\partial V_2)\\ \hat{\mathbf{v}}^{t}(x\in\partial V_1)\\ \hat{\mathbf{t}}^{sc}(x\in\partial V)\end{pmatrix}=\{\mathbf{B}'\}. \tag{7.26}$$

By solving these matrix equations and employing the solution in the interface conditions (7.13-20), the unknowns, $\hat{\mathbf{u}}^{sc}, \hat{\mathbf{t}}^{sc}, \hat{\mathbf{v}}^{t}, \hat{\mathbf{s}}^{t}$, can be evaluated.

7.4 Validation of BEM Simulation by Analytic Model

Analytic solutions were used to validate the boundary element method approach. The solution for the scattering response of an incident plane shear wave (as presented in Section 7.2) was used for validation. Figure 7.4 displays seven locations where the total field response was calculated. The parameters for this simulation are presented in Appendix A. Comparisons are shown in Figures 7.5(a)-(b) between the 'exact' and BEM solutions for the in-plane radial and tangential displacement respectively. Excellent agreement was found between the exact and BEM solutions.

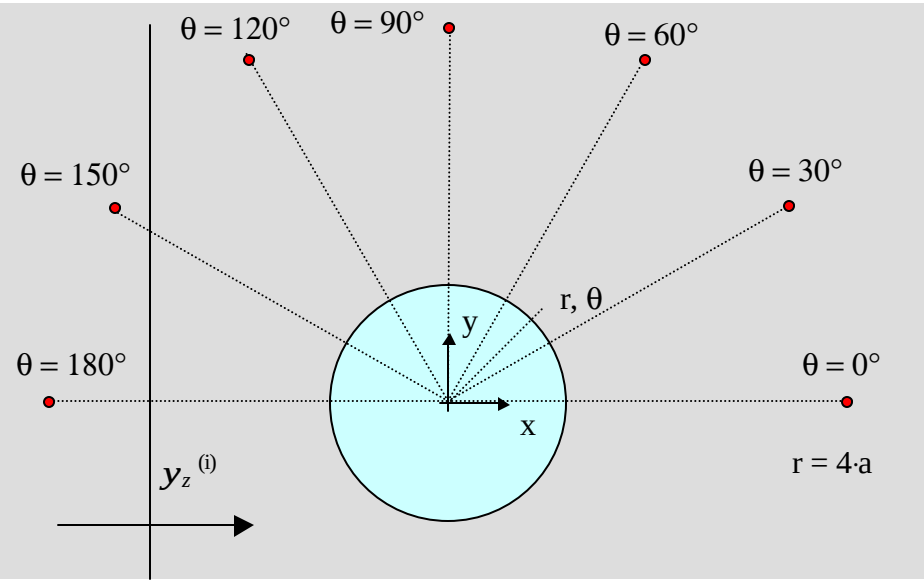

Figure 7.4. Diagram of location of external points for comparison of BEM and analytic in-plane displacement magnitudes (r = 4·a).

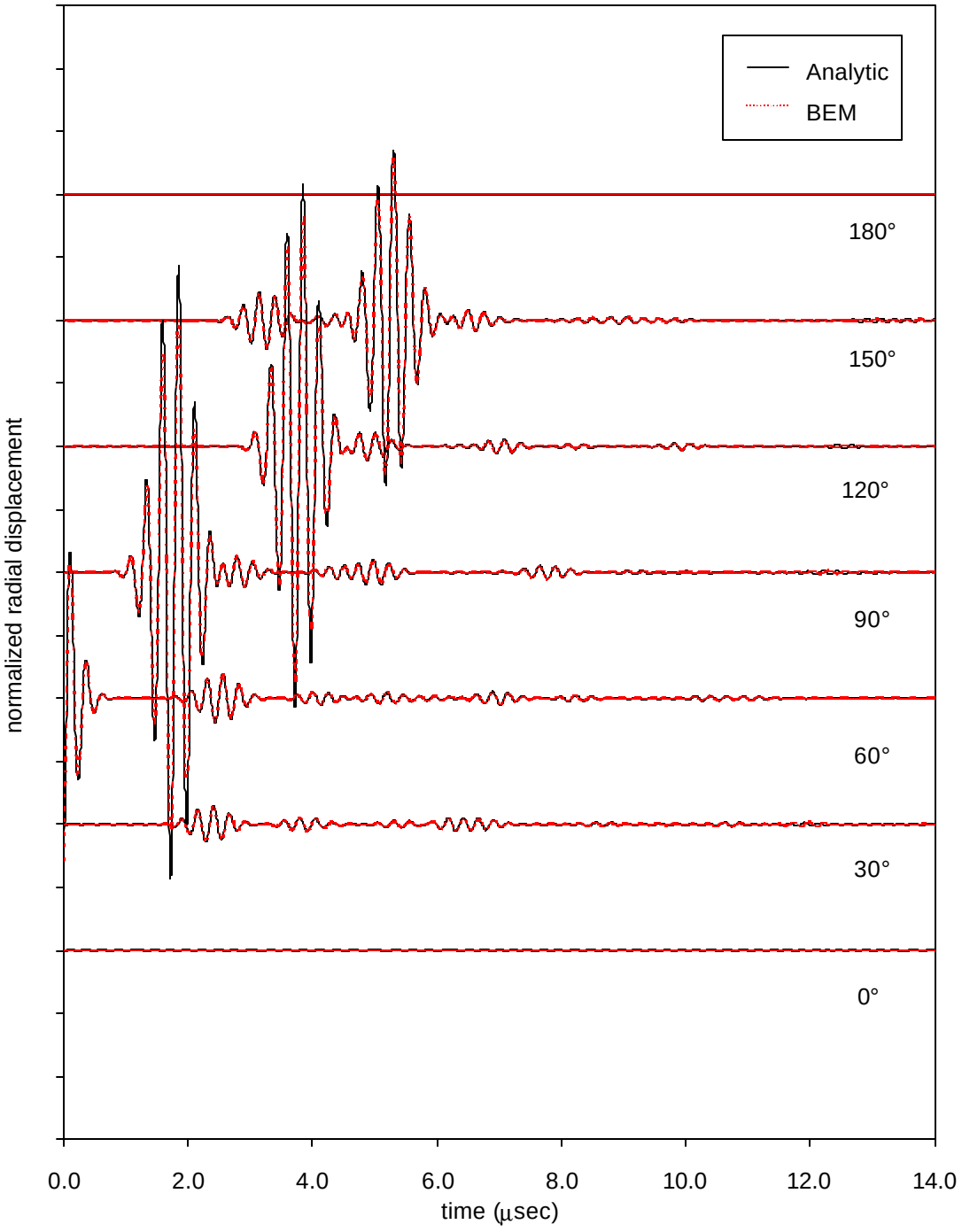

Figure 7.5(a). Comparison of analytic and BEM solutions for the in-plane radial displacement at seven radial locations for an incident plane 5.0 MHz shear wave.

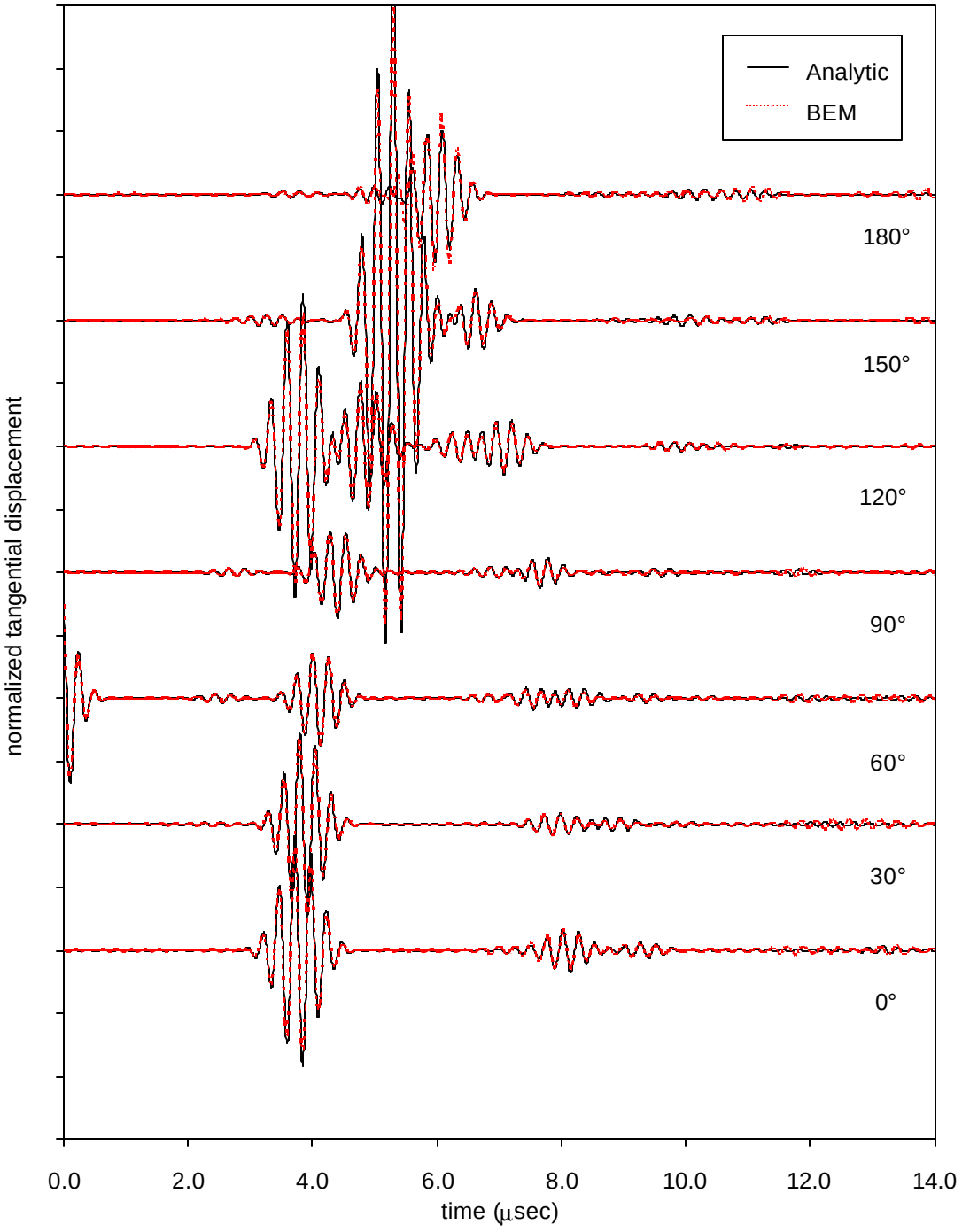

Figure 7.5(b). Comparison of analytic and BEM solutions for the in-plane tangential displacement at seven radial locations for an incident plane 5.0 MHz shear wave.

7.5 Discussion of Analytic Model Results for Plane Wave Incidence

Analytic solutions for the total displacement field response to an incident in-plane plane shear wave on a 3/16" diameter rib clip hole containing an aluminum insert in smooth contact are shown as contour plots in Figure 7.6 for nine time steps, τ = 0,1,2,3,4,5,6,7,8. The properties for the infinite elastic solid (riser) and the elastic insert (fastener) are given in Appendix A. To facilitate the description of the scattering of waves for this case, diagrams displaying the ray traces for selected incident rays are used. Figure 7.7 displays the scattering of multiple incident rays within the cylindrical elastic insert. Since the difference in the material properties of the two aluminum alloys is negligible, the angle of transmission for shear waves in the elastic insert is essentially equal to the incident shear wave angle made with the normal to the hole surface for most incident angles. Thus, little refraction of the initial shear wave into the insert is shown in Figure 7.7. From these incident rays, Figures 7.8 displays four of the significantly scattered rays from a hole with an elastic insert. These four diagrams will be used in the discussion.

As the incident shear plane wave impinges on the smooth boundary between the medium and the insert, specular reflection and transmission of both longitudinal and shear waves initially occur. Figure 7.8(a) shows the corresponding ray diagram. Clearly, specular reflection as shear waves represents the most significant signal returning to possible locations of measurement transducers. In addition, the transmitted shear waves

can be observed propagating within the elastic solid, reflecting off of the interface initially, and then re-transmitting back into the elastic medium. Figure 7.8(b) and 7.8(c) show two cases for the re-transmitting into the surrounding solid of these waves to which propagate in the direction of the measurement transducers. Due to the smooth boundary condition, 'leaky' Rayleigh waves are also generated and propagate about the cylindrical hole. Figure 7.8(d) shows the ray diagram for the propagation of 'leaky' Rayleigh waves. These waves generate circumferential shear waves that also propagate in the direction of the measurement transducers. For this aluminum insert case, the 'leaky' Rayleigh wave follows after the re-transmitted shear waves from the insert.

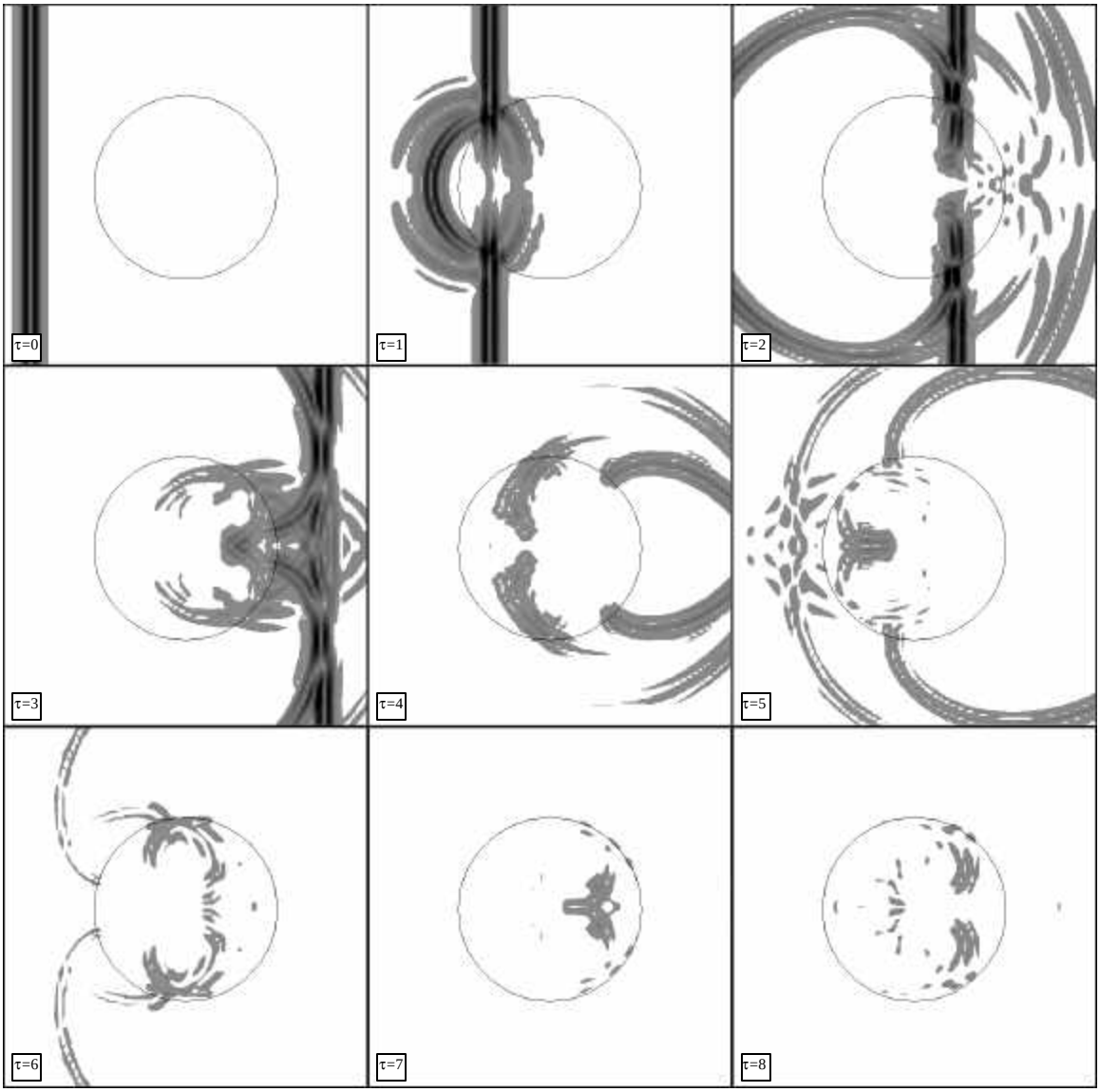

Figure 7.6. Contour plots of the total displacement field response to an incident in-plane shear plane wave on a 3/16" diameter rib clip hole containing an aluminum insert in smooth contact - for nine time steps, $\tau = 0,1,2,3,4,5,6,7,8$.

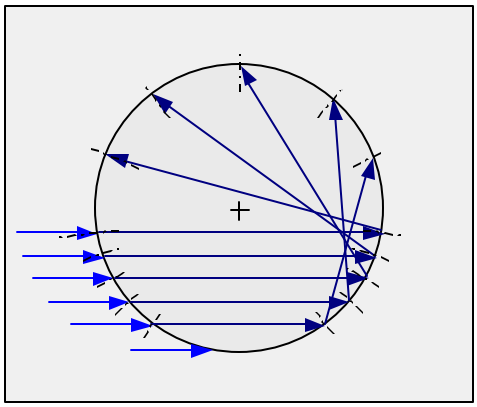

Figure 7.7. Diagram of reflection of multiple incident shear rays within an elastic insert.

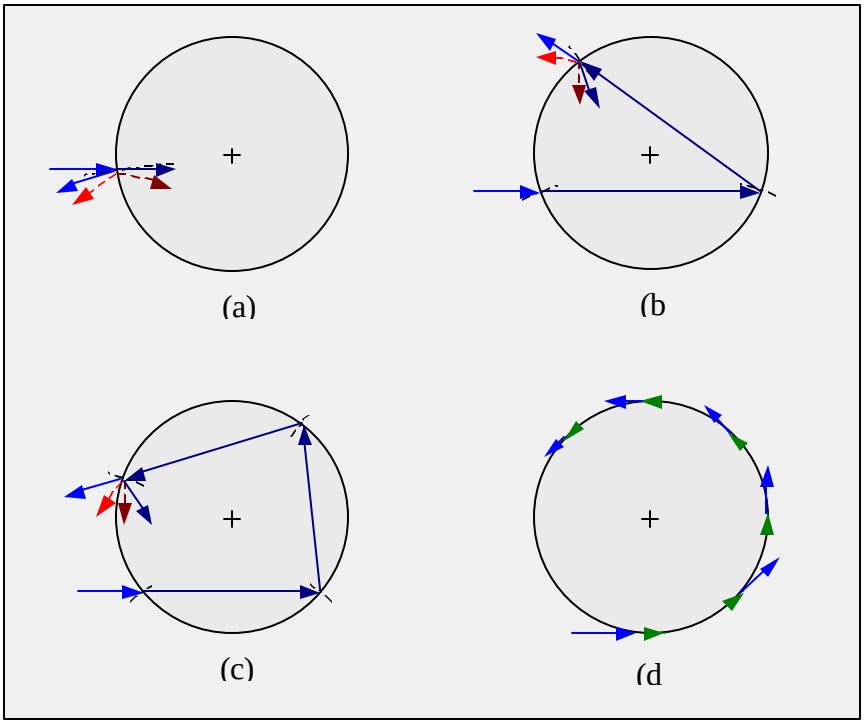

Figure 7.8. Diagram of significantly scattered rays for transducer measurement from hole with elastic insert: (a) specular longitudinal and shear reflection, (b) retransmitted case 1 from shear wave transmisson, (c) retransmitted case 2 from shear wave transmission, (d) generation of circumferential shear waves from 'leaky' Rayleigh wave propagation.

7.6 Discussion of BEM Simulations for Incidence of Transducer Signals

The BEM solutions for the total displacement field generated by an incident in-plane shear wave on a 3/16" diameter rib clip hole containing an aluminum insert in smooth contact, are shown as contour plots in Figure 7.9 and 7.10 for nine time steps, τ = 0,1,2,3,4,5,6,7,8. Figure 7.9 and 7.10 display the no-notch and 0.070'' top notch cases respectively. Simulation parameters are given in Appendix A.

For the no-notch case shown in Figure 7.9, similar results with respect to the analytic case are observed. Initially, specular reflection and transmission of longitudinal and shear waves occur. Significant specular reflections return to the possible locations of the measurement transducers. The transmitted shear waves can be observed propagating within the elastic solid, reflecting off of the boundary initially, and then re-transmitting back into the elastic medium. Figure 7.8(b) and 7.8(c) show two cases for the re-transmitting of these waves from the insert to propagate in the direction of measurement transducers as observed in Figure 7.9. Figure 7.11 shows a related signal, ray trace (e), which begins above the center of the hole but retransmits a signal below the center of the hole in the direction of the pitch transducer. These signals are observed to significantly contribute to the measured transducer response. Due to the interface condition by which the tangential displacements are loosely coupled via a weak tangential stiffness, 'leaky' Rayleigh waves are also generated to propagate about the cylindrical hole. Figure 7.8(d) shows the ray diagram for the propagation of 'leaky' Rayleigh waves. These waves

generate circumferential shear waves that also propagate in the direction of the measurement transducers. For the aluminum insert case, these waves lag the re-transmitted shear waves from the insert.

To facilitate the understanding of the scattering of waves for the notch case, diagrams displaying the ray-tracing for selected incident rays are used. Figures 7.12 displays three of the significant scattered ray traces, (f,g,h), for transducer measurement of signals from a hole with an elastic insert and a top notch.

Initially for the notch case, shown in Figure 7.10, similar results are observed as compared to the no-notch case. First, specular reflection and transmission of longitudinal and shear waves occurs. The resulting specular shear reflection returns to possible locations of the measurement transducers. Again, the transmitted shear waves can be observed propagating within the elastic solid, reflecting from the boundary initially, and then re-transmitting back into the elastic medium. Additional signals are observed when the transmitted shear signal becomes incident at the interface location of the notch. Scattering from this location occurs in the form of shear and longitudinal waves within the elastic insert. These signals re-transmit into the elastic medium where they may be detected by transducers. The ray tracing for this case is shown in Figure 7.12(g). Again, 'leaky' Rayleigh waves are also generated and propagate about the cylindrical hole. Reflection of the 'leaky' Rayleigh wave by the notch is clearly observed in Figure 7.10. As the 'leaky' Rayleigh wave propagates back from the notch, circumferential shear waves are generated which can be detected by the pitch transducer. Figure 7.12(f) shows the ray tracing for this case. Clearly, significant measurable

differences in the scattering responses from the no-notch and the notch cases exist. Lastly, measurable signals are observed when the transmitted shear signal becomes incident at the interface location of the notch and diffraction occurs producing a transmitted 'leaky' Rayleigh wave propagating about hole. Figure 7.12(h) shows the ray tracing for this case. Although the magnitude of this signal is smaller than the 'leaky' Rayleigh wave for the no-notch case, this signal will add noise to the pitch-catch measurement used for top crack detection.

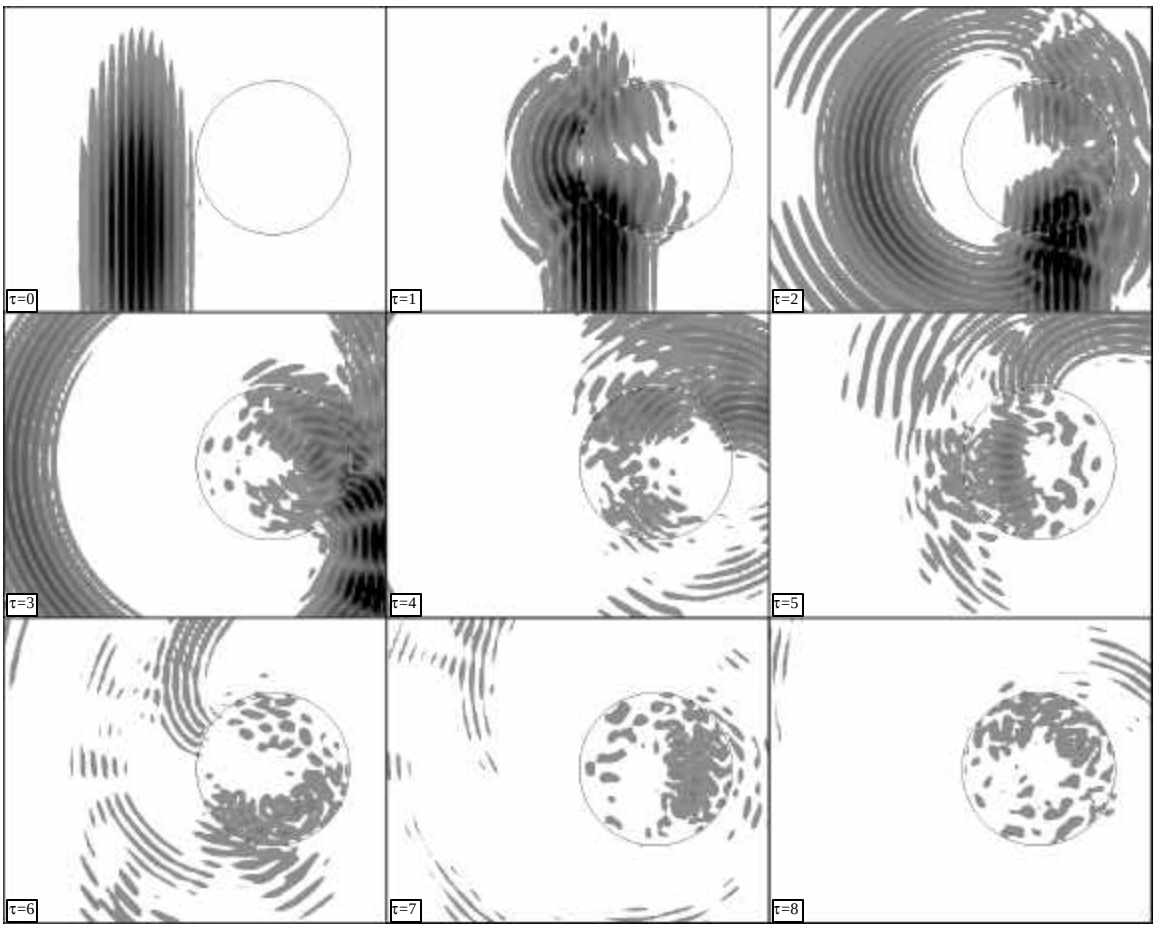

Figure 7.9. Contour plots of the total displacement field generated by an incident in-plane shear pulse on a 3/16" diameter rib clip hole with no crack and containing an aluminum insert – elastic contact between insert and hole (smooth contact; K_L = 1e17, K_T = 1e11) - for nine time steps, τ = 0,1,2,3,4,5,6,7,8.

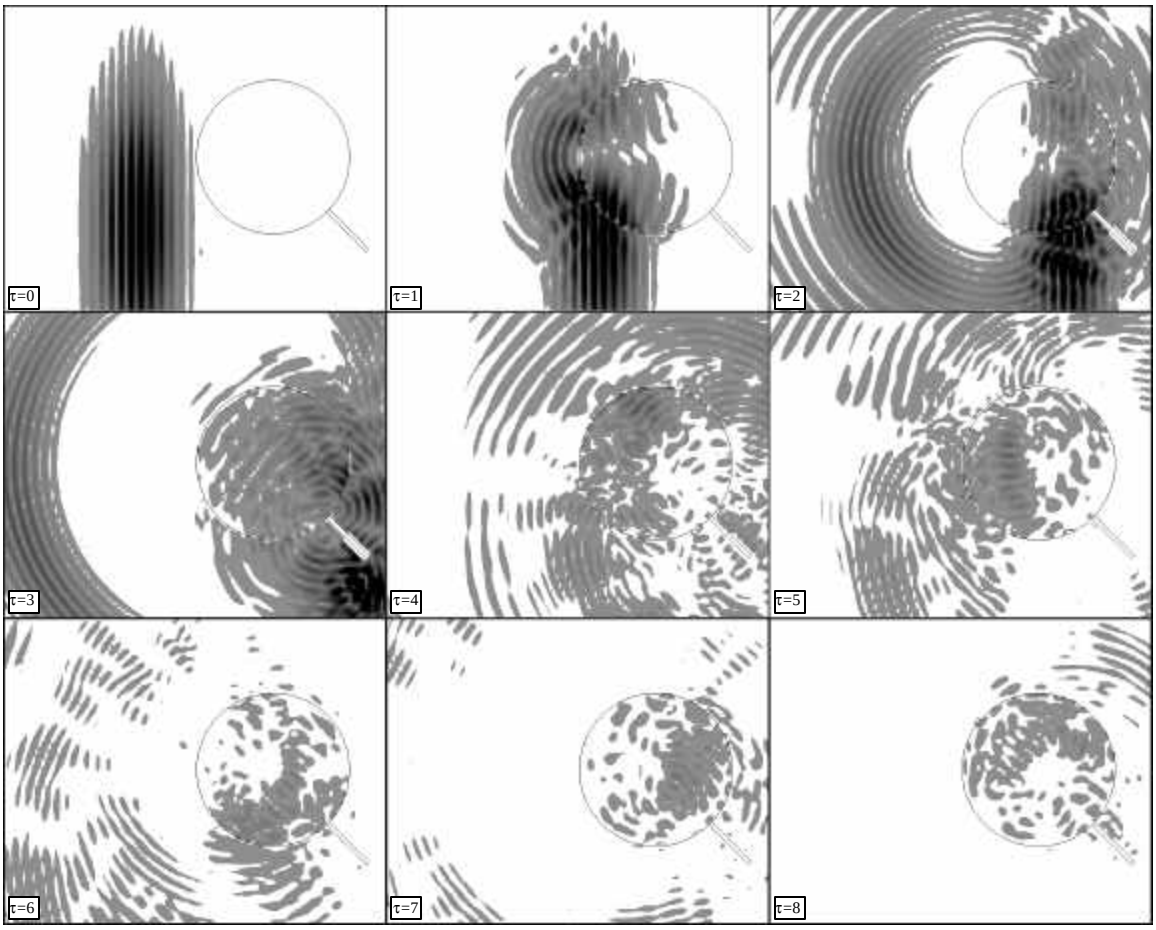

Figure 7.10. Contour plots of the total displacement field generated by an incident in-plane shear pulse on a 3/16" diameter rib clip hole with a 0.070" notch and containing an aluminum insert – elastic contact between insert and hole (smooth contact; K_L = 1e17, K_T = 1e11) - for nine time steps, τ = 0,1,2,3,4,5,6,7,8.

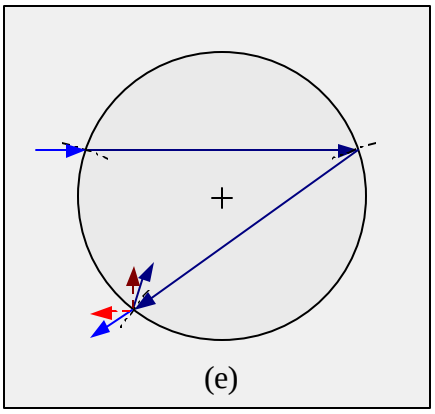

Figure 7.11. Diagram of significant scattered rays for transducer measurement of signals from a hole with an elastic insert: (e) retransmitted case 3 from shear wave transmission.

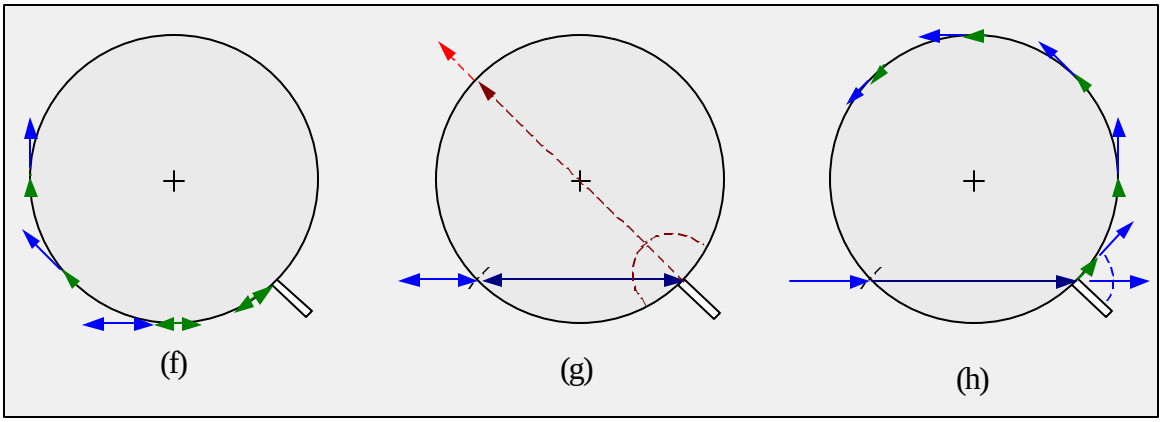

Figure 7.12. Diagram of significant scattered rays for transducer measurement of signals from a hole with an elastic insert and a top-notch: (f) circumferential shear wave from reflected 'leaky' Rayleigh wave, (g) diffracted longitudinal and shear waves through insert from transmitted shear wave in insert at notch, (h) circumferential shear wave from 'leaky' Rayleigh wave generated by diffraction of transmitted shear wave at notch.

Figures 7.13 and 7.14 display plots of the pulse-echo and pitch catch measurements respectively for the C-141 rib clip hole case. Experimental and simulated signals are compared for four cases: no insert and no top notch, no insert with 0.070 in. top notch, with elastic insert and no top notch, and with elastic insert and with top notch. Details concerning the parameter for the experiment and simulation are presented in Appendix A.

A few qualifications must first be made about the comparison of the plots. First, the experimental data was acquired using an 8 bit ADC. Significant gain was used to improve the resolution of the reflected and transmitted 'leaky' Rayleigh wave signals for improved inspection purposes. However, a portion of the specular reflection signal is saturated. Since the primary goal of this comparison is to present the key features of these signals from an inspection perspective, an approximate matching of the simulated signals with the experimental results was performed. Second, there exist significant secondary signals following the primary specular signal that may obscure the interpretation of the inspection signals of interest. These secondary signals are generated by sidewall reflections of the main specular signal within the finite width riser. From experimental and simulated studies, these signals are typically about 10-20% of the magnitude of the primary signal and are located about 0-3 μsec after in time. The magnitude and location in time are dependent upon the alignment of the transducer with respect to the riser, and the location and geometry of the hole. Since rib clip holes are deeper within the riser, and the hole diameter is reduced (with respect to the weep hole), sidewall reflected signals are a greater concern. At this point, inspection signals are

desired which do not coincide with these sidewall reflected signals. This issue will be further addressed in the next section. After factoring out these two issues concerning the experimental data, good agreement was generally found between the experimental and simulated signals.

For the pulse-echo measurements shown in Figure 7.13, the presence of the reflected 'leaky' Rayleigh wave signal is the primary signal indicator for the existence of a top notch. For the simulated results, there is about a 40% reduction in the magnitude of the reflected 'leaky' Rayleigh wave signal. This change is primarily due to loss into the elastic insert. Superposition with other re-transmitted signals from the insert also may effect the magnitude. In addition, at this location in time, there do exist both re-transmitted signals from the insert and sidewall reflected signals from the main specular reflection. Although these signal are generally small with respect to the reflected 'leaky' Rayleigh wave signal, they will reduce the detection performance of the algorithm. A single inspection location of 0.120 in. from the specular reference was presented in Figure 7.13. Further investigations into locating the transducer for optimal pulse-echo inspection for top cracks will be performed in the next section.

One final pulse-echo signal of note is the re-transmitted signal initially scattered from the interface location at the notch as shown in Figure 7.12(g). The simulated signal for the insert and notch case indicates the existence of this signal prior to the reflected 'leaky' Rayleigh wave. However, due to the small magnitude of this signal and the location of the signal within the range of the specular sidewall signals, it would be very difficult to incorporate this signal into a robust top crack detection scheme.

For the pitch-catch measurements shown in Figure 7.14, the presence of the transmitted 'leaky' Rayleigh wave signal is an indicator for the existence of a top notch. For the simulated results, there is about a 40% reduction in the magnitude of the reflected 'leaky' Rayleigh wave signal. This change is partly due to loss into the elastic insert. Superposition with other re-transmitted signals from the insert also may effect the magnitude. Although the specular sidewall signals may not be as significant in the time of flight interval of the transmitted 'leaky' Rayleigh wave, the re-transmitted signals from the insert are more significant. Both the re-transmitted shear wave from the insert (b), and the circumferential shear wave from 'leaky' Rayleigh wave generated by diffraction of transmitted shear wave at the notch coincide in time with the transmitted 'leaky' Rayleigh wave. Although these signals are generally small with respect to the reflected 'leaky' Rayleigh signal, they will affect the detection performance of the algorithm. As was previously proposed for the empty weep hole case, a procedure incorporating both the pulse-echo and pitch-catch signals would best determine the existence of top cracks for the C-141 rib clip hole case.

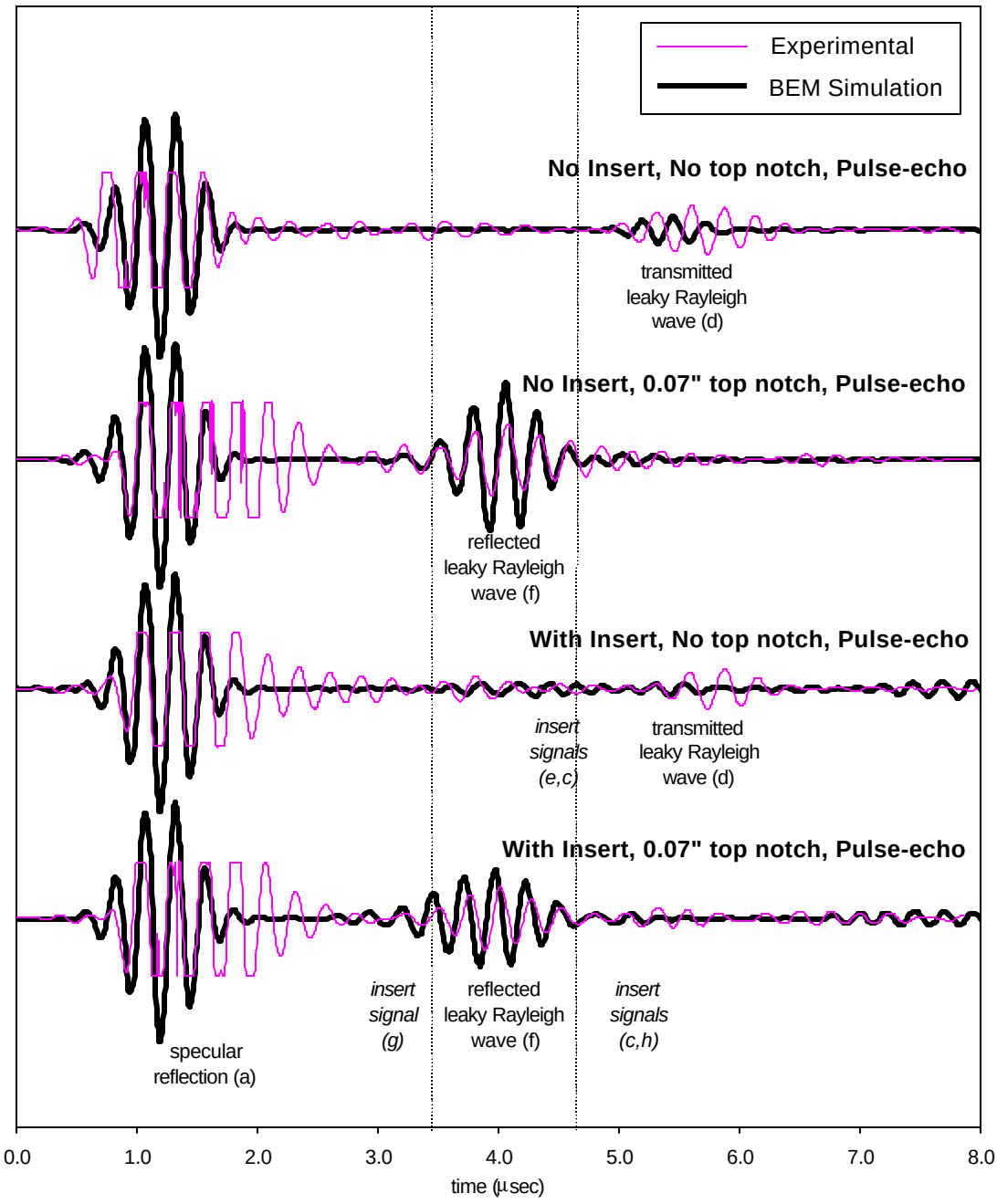

Figure 7.13. Simulated and experimental pulse-echo signals for a transducer signal incident on a rib clip hole – with and without an insert and/or a notch.

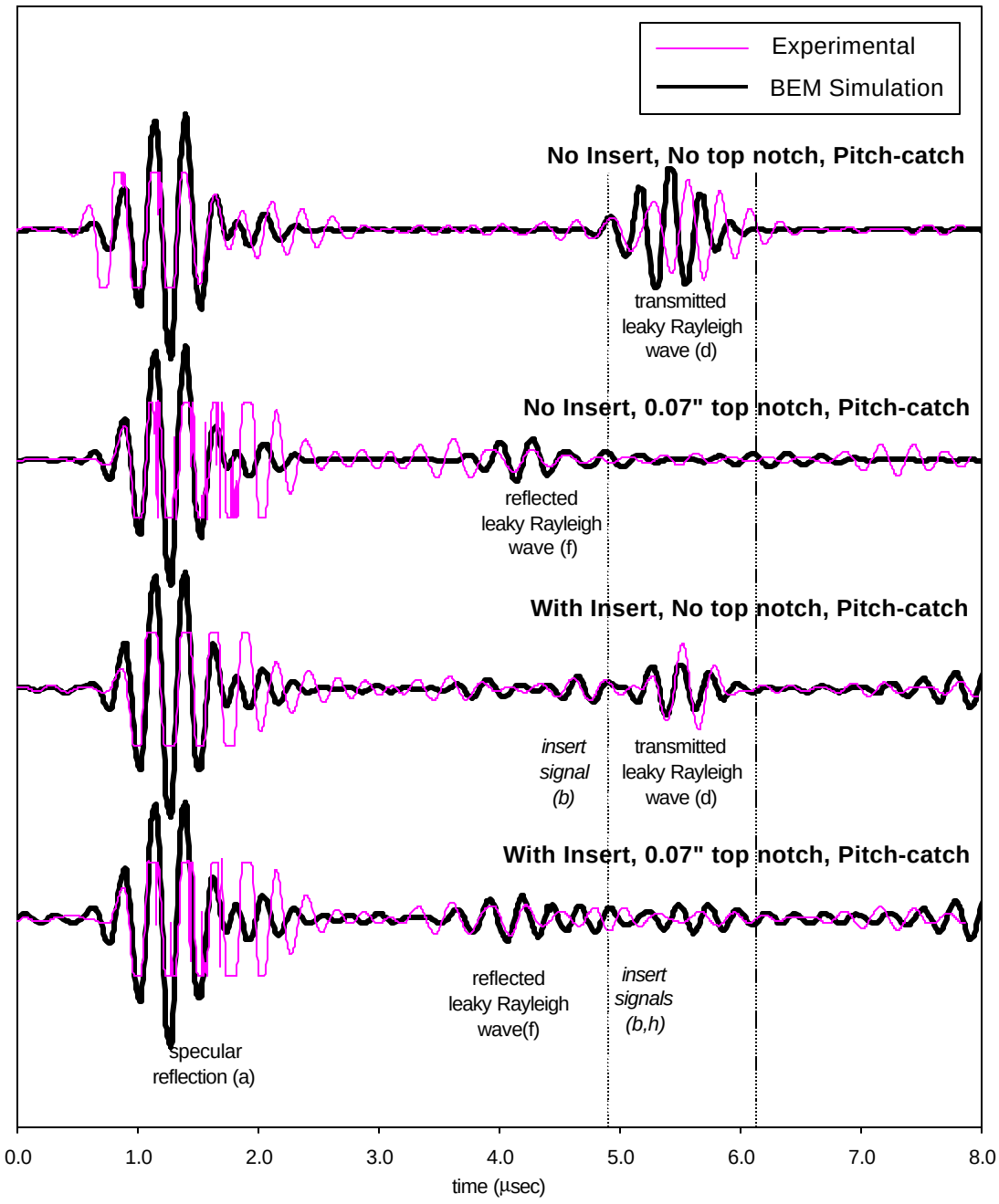

Figure 7.14. Simulated and experimental pitch-catch signals for a transducer signal incident on a rib clip hole – with and without an insert and/or a notch.

7.7 Parametric Studies for Top Notch Detection

From the simulated results and the experimental studies, three possible sources of noise can be classified. The first source of noise is due to reflected sidewall signals from the hole specular reflection. Two features of the inspection problem contribute to the formation of this signal. First, the curvature in the transducer beam propagating in the riser produces sidewall reflections. Secondly, the thin riser section and fillet further promote the formation of sidewall reflections (see Figure 1.2 for a view of a riser cross-section.) From observations of the experimental pulse-echo signals (shown in Figure 7.13) and from rudimentary ray-tracing calculations, these signals are found to follow the hole specular reflection signal primarily between 0 to 3 μsec. The magnitudes of these signals are typically 10 – 20 % of the magnitude of the specular reflection signal. Due to their location in time, they are expected to more greatly affect the pulse-echo measurement. The second source of noise is due to scattered signals from within the insert. Figure 7.13 and 7.14 show the presence of these signals for both the experimental and simulated data. From these observations, this second source of measurement noise will more greatly affect the pitch-catch measurement. The third source of noise is due to random noise found in the inspection system. This noise should generally be independent of the measurement and transducer location.

The BEM model was used to determine the best transducer location to maximize the signal to noise ratio for these noise sources. Due to the close proximity of the pulse-

echo measurement gate to the time of flight of the reflected sidewall signals, minimizing the magnitude of the reflected sidewall signal with respect to the reflected 'leaky' Rayleigh wave signals is of interest. The pulse-echo response was simulated for various transducer locations and notch lengths. Figure 7.15 displays the results for two transducer locations (0.120'' and 0.220'' back from specular reference) and for the no-notch and 0.070'' notch cases. As the transducer is moved further from the hole, although the reflected 'leaky' Rayleigh wave signal decreases in magnitude, the relative magnitude of the reflected 'leaky' Rayleigh wave signal with respect to the specular reflection signal actually increases. Since the magnitude of the sidewall reflected signal is directly related to the magnitude of the specular reflection signal, the signal (reflected 'leaky' Rayleigh wave) to noise (sidewall reflected signal) ratio is expected to improve when the transducer is moved from 0.120'' to 0.220''. Further movement of the transducer away from the reference location will eventually lead to a reduced signal to noise ratio if the significant contribution to noise is due to the inspection system. The transducer location of 0.220'' from the hole reference was found to be a good position for acquiring pulse-echo response signals.

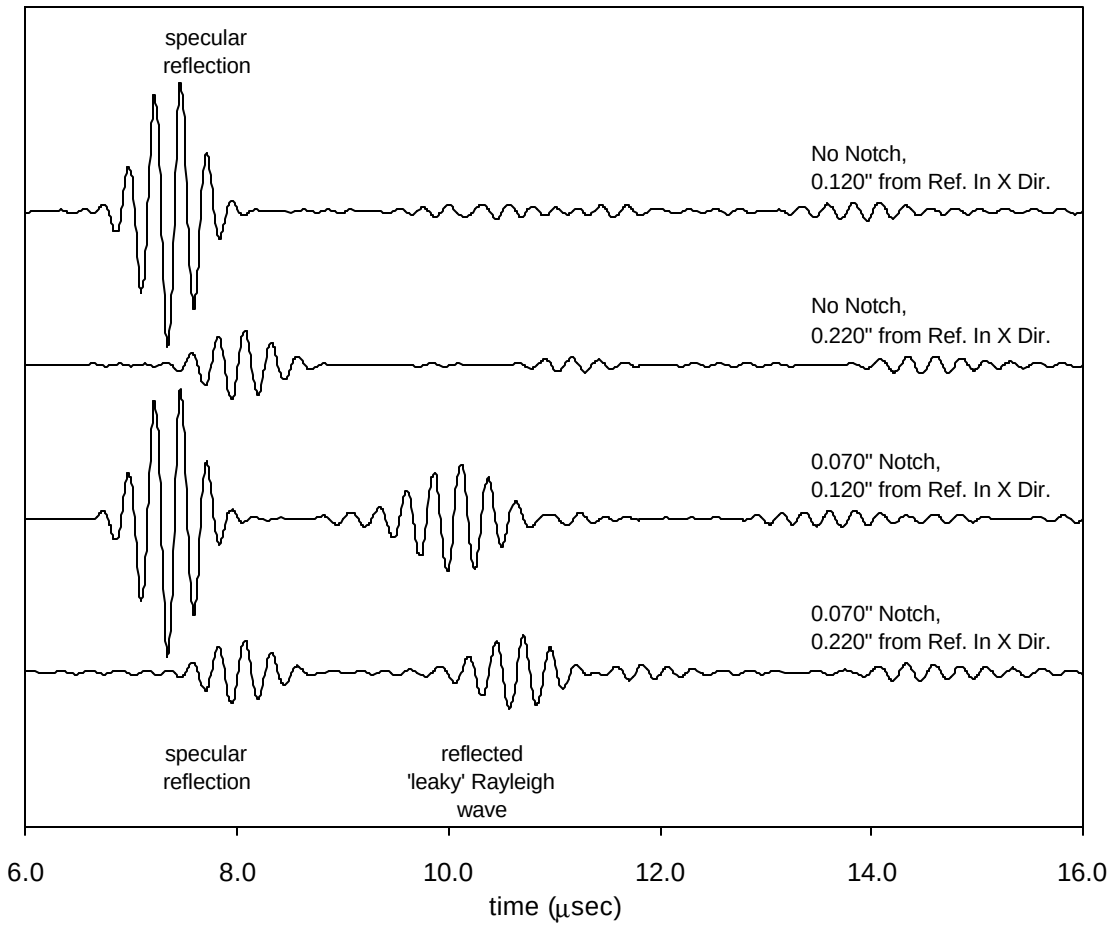

Figure 7.15. Simulated pulse-echo signals for a rib clip hole - two transducer locations along the riser length (in X-direction), and no-notch and notch conditions shown.

Other parameters that were investigated using the BEM simulation were the material properties of the elastic insert. Typically, aluminum rivets are used for C-141 rib clip holes and C-130 beam cap holes. However, in one C-130 beam cap section that was examined, steel inserts were found. Although not desirable from the point of view of corrosion, steel inserts may exist in the field and thus the inspection algorithm should be sufficiently robust for this possible inspection condition.

BEM solutions of the total displacement field response to an incident in-plane shear wave on a 3/16" diameter rib clip hole containing a steel insert in smooth contact are shown as contour plots in Figure 7.16 for nine time steps, $\tau = 0,1,2,3,4,5,6,7,8$. The parameters for the simulation are given in Appendix A. These plots were compared to the results for an aluminum insert, shown in Figure 7.9.

Clearly, significant features that can be measured for the aluminum insert case are not present for the steel insert case. The magnitude of the 'leaky' Rayleigh wave is both reduced and obscured within the re-transmitted signals from the insert. Although the shear wave speed for steel is comparable to aluminum, the difference in material density produces the differences between the two contour plots.

Figure 7.17 displays comparisons of the pulse-echo and pitch-catch signals for the aluminum and steel insert and for both the no-notch and 0.070'' notch cases. As observed in the contour plots, the transient signals for the steel insert case do not indicate the features used for classification of the signals for the aluminum insert case. The steel case signals are characterized by stronger re-radiated signals from the insert with an

obscured ‘leaky’ Rayleigh wave signal. Although classification features may exist, the likelihood that they are robust enough for in-field measurement is unlikely.

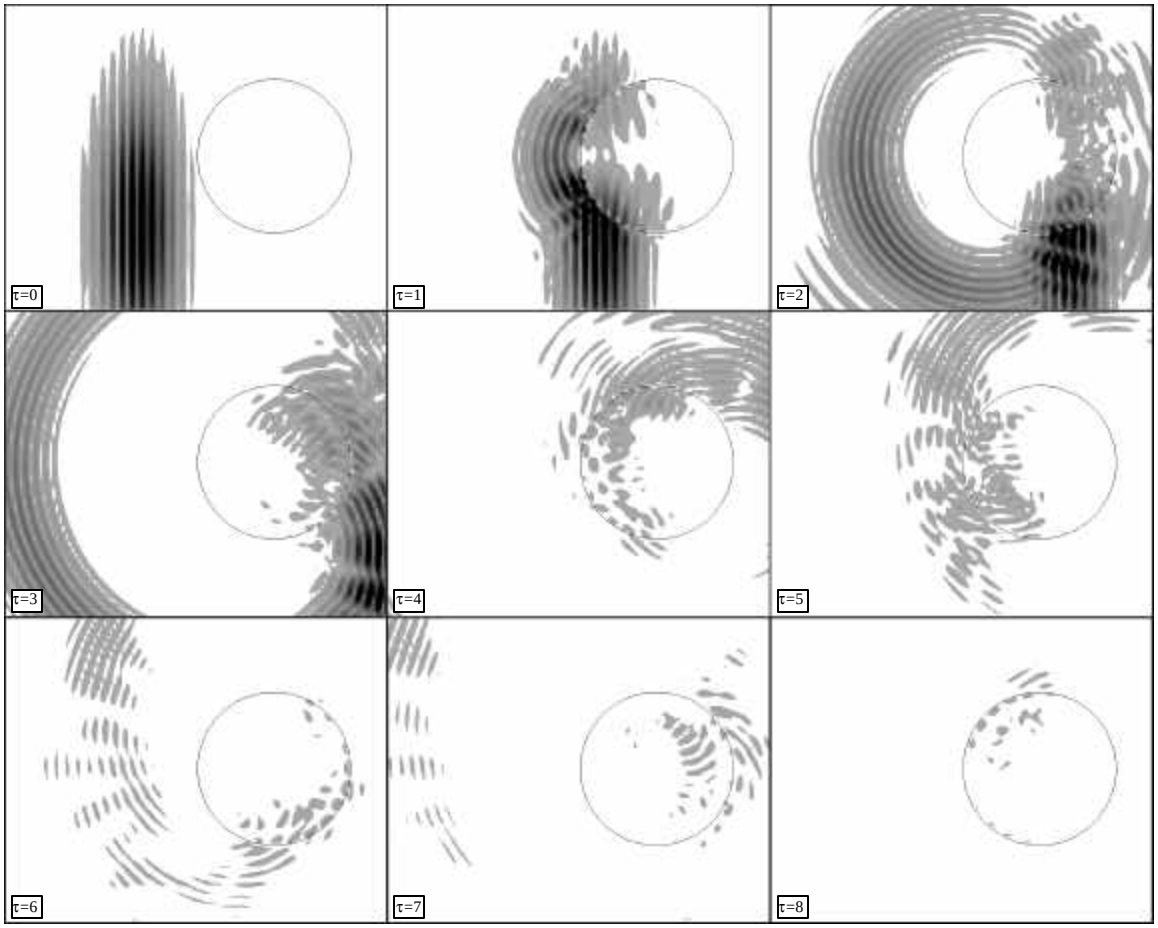

Figure 7.16. Contour plots of the total displacement field response to an incident in-plane shear pulse on a 3/16" diameter rib clip hole with no crack and containing a steel insert with elastic contact between insert and hole (smooth contact; K_L = 1e17, K_T = 1e11), for nine time steps, τ = 0,1,2,3,4,5,6,7,8.

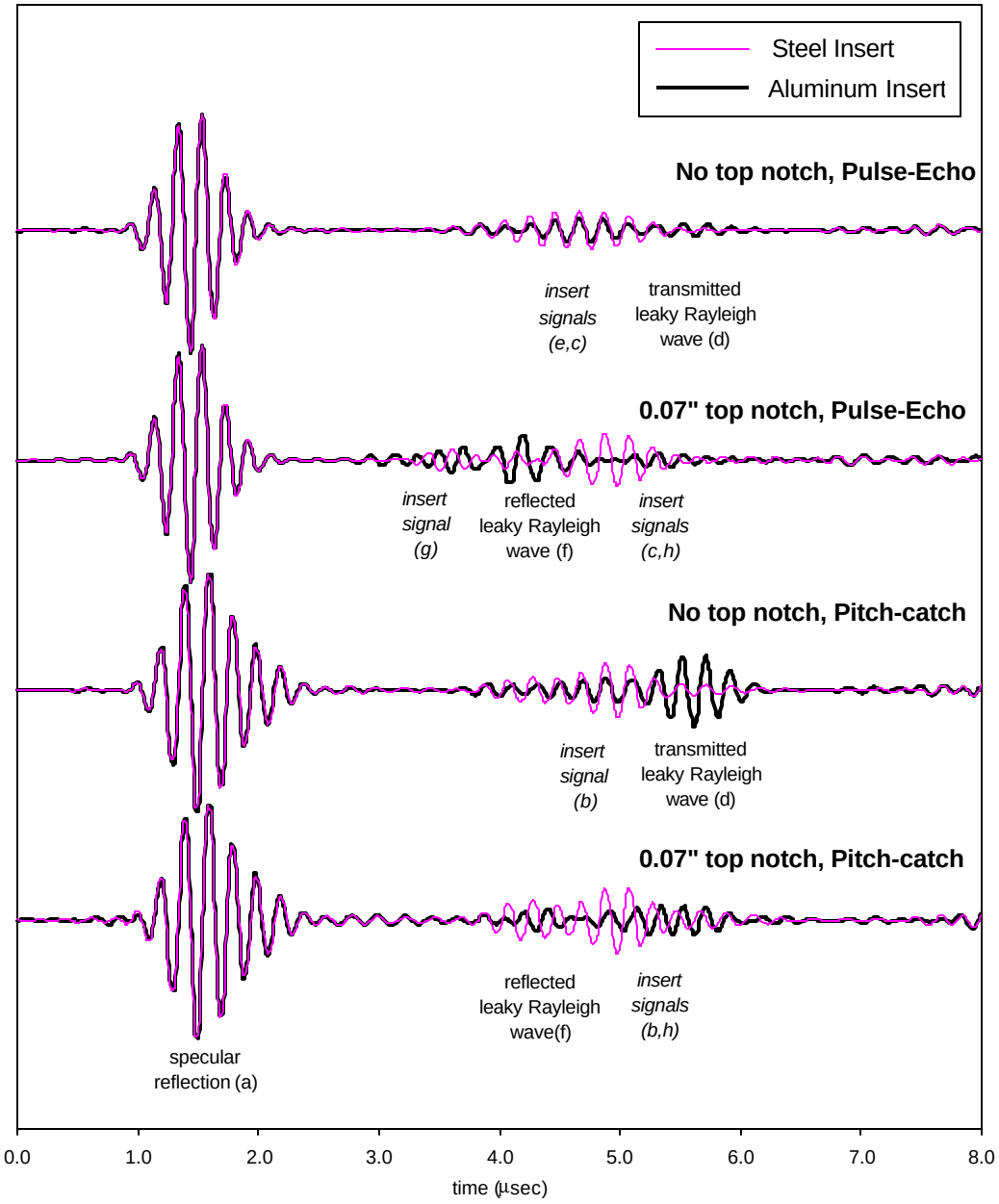

Figure 7.17. BEM solution for pulse-echo and pitch-catch signals for an incident transducer signal on a hole comparing the response for the aluminum and steel insert cases (trans. -0.120" from specular ref.)

7.8 Proposed Algorithm for Top 'Corner' Notch Detection

Weep hole ultrasonic inspection techniques described earlier in this Dissertation addressed the inspection of 0.070'' 'through' cracks in a 0.200'' riser section. As part of the current Air Force initiative to develop an ultrasonic technique for the detection of fatigue cracks in holes containing fasteners, the challenging inspection goal of 0.070'' × 0.070'' 'corner' crack detection was proposed as a measure of algorithm success. To better understand the 'corner' crack inspection problem, an accurate model would be desirable. Unfortunately, the 2D BEM simulation inadequately represents this inspection problem. Due to the lack of the necessary development time and the computation hardware required for an accurate 3D simulation, the decision was made to use experimental studies to better understand the inspection problem.

Figures 7.18 and 7.19 display pulse-echo signals at 10 locations incremented 0.020'' along the width of the riser for no-notch and through-notch cases respectively. Similarly, Figures 7.20 and 7.21 display pitch-catch signals for no-notch and through-notch cases respectively. Significant variation in the magnitude of the classification signals is observed as the transducer location is varied along the riser section. Secondly, significant variation in the magnitude and location of the sidewall reflected signal is also observed. To best address this variation using a classification algorithm, a three-layer inspection algorithm design is proposed. The algorithm diagram is shown in Figure 7.22.

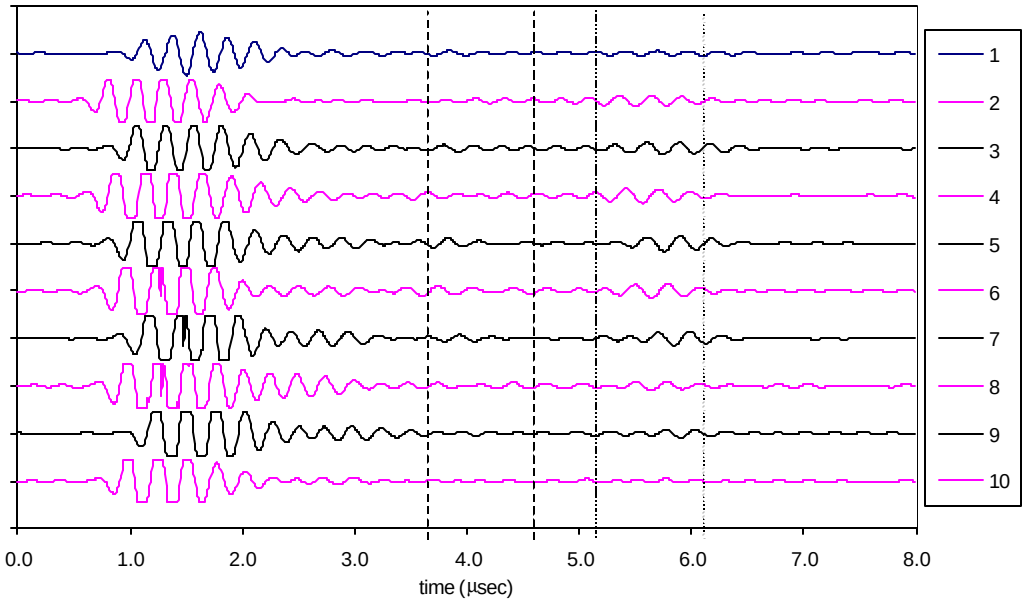

Figure 7.18. Pulse-echo signals from 10 points along riser width – no notch case.

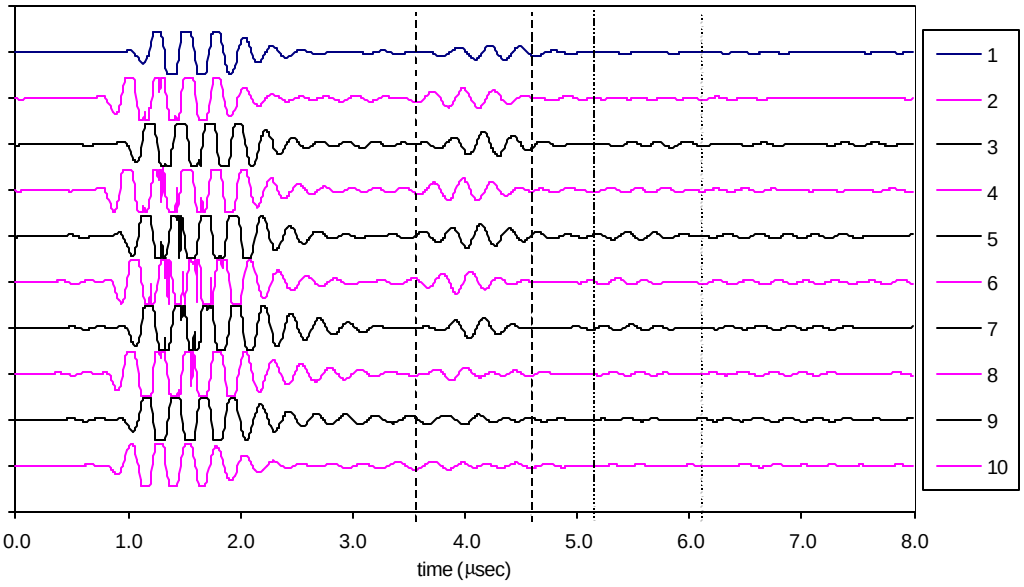

Figure 7.19. Pulse-echo signals from 10 points along riser width – 'through' notch case.

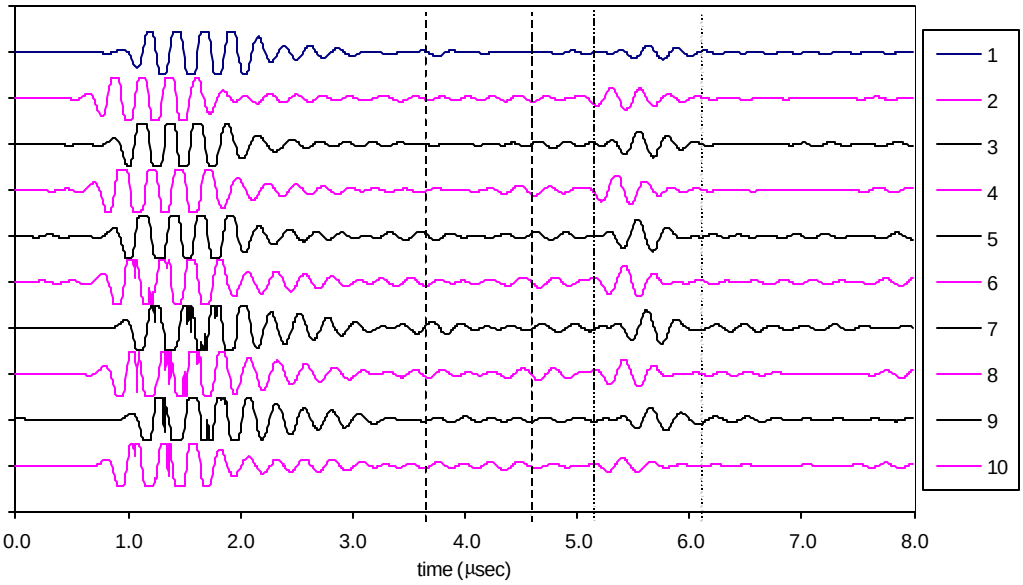

Figure 7.20. Pitch-catch signals from 10 points along riser width – no notch case.

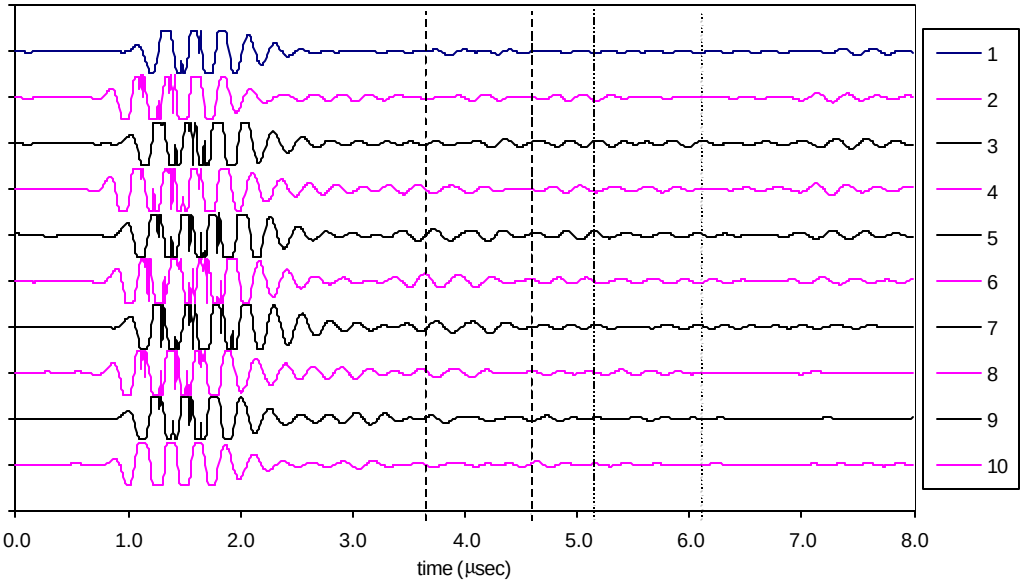

Figure 7.21. Pitch-catch signals from 10 points along riser width – 'through' notch case.

Optimization of the through-notch, right ‘corner’ notch, and left ‘corner’ notch classification algorithms will be explored for these inspection cases in the next Section.

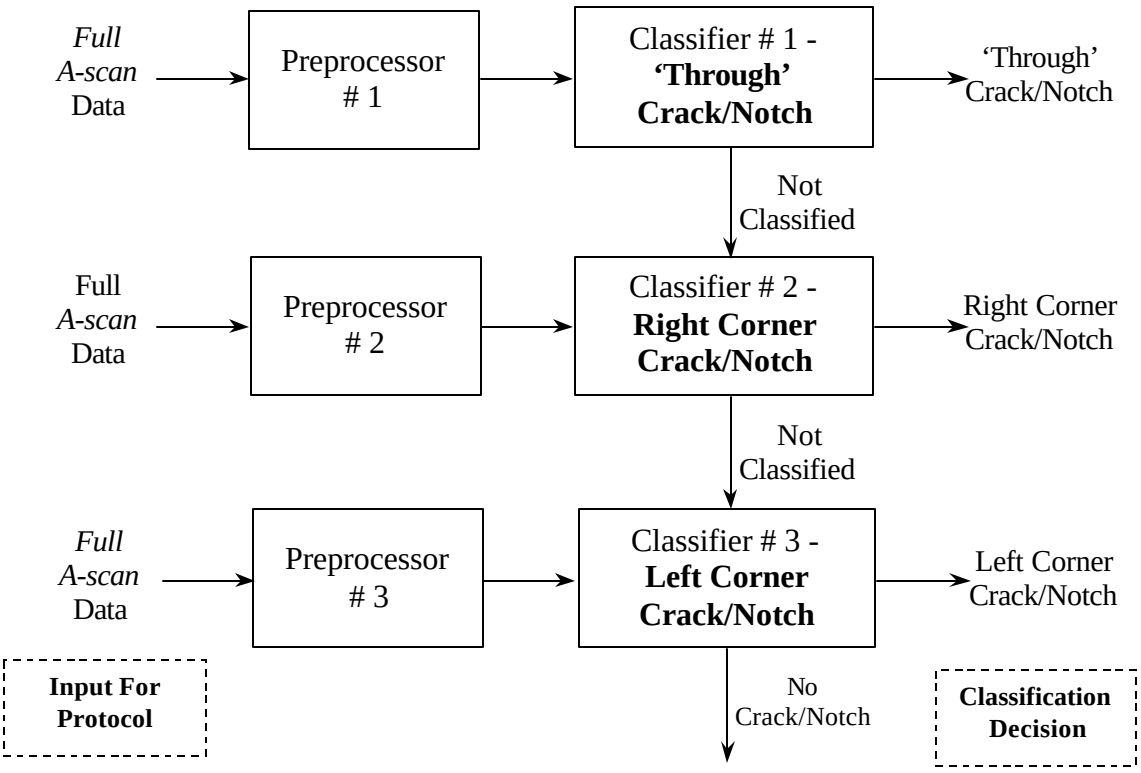

Figure 7.22. Flow chart for top crack detection procedure.

7.9 Optimization of Top Notch Classification Procedure Using Genetic Algorithms

Often, straightforward inspection procedures are not viable due to geometric complexity or uncontrolled variation of the inspection location. To implement more elaborate procedures for these inspection problems, automation of the signal processing and classification call has been used [14,15,22]. The primary emphasis for implementing an automated inspection procedure is to minimize inspection error and to reduce classification variation between inspectors.

During the implementation phase, optimization of the automated inspection procedure is desired. Primarily, expert knowledge through experimentation and modeling is relied upon to set the majority of the parameters. For more complex problems, the setting of inspection parameters using expert knowledge may not be ideal when key classification features in the data set are poorly understood. An example is top 'corner' crack detection for the C-141 rib clip hole. Conversely, given the large number of parameters, optimization is often difficult. Classical optimization methods are typically prone to missing global minima due to nonlinearity in the domain while exhaustive search techniques require excessive computational time.

Genetic algorithms have been proposed as a means for handling complex optimization problems in reasonable solution times [78,79]. Optimization incorporating genetic algorithms consist of the following steps: coding of the input parameters into an individual binary code, generation of the initial population as sets of the individual code,

calculation of the fitness measure for each individual code in the population, crossover between two selected individual codes, mutation of selected individual codes at random bit locations, and repetition until the fitness measure criteria is satisfied. Genetic algorithms have been used in the field of non-destructive evaluation for sensor design optimization [80], improvements in contour fitting algorithms in image analysis [81], optimization of multiple data fusion [82], evaluation of material properties through inverse optimization problem [83], and optimization of signal deconvolution [84]. As an extension of these works, genetic algorithms may also be used to discover new or more robust features for inspection.

The strategy presented here is to apply genetic algorithms in order to optimize the inspection algorithm and simultaneously explore specific aspects of the inspection procedure that may indicate using alternative classification approaches. For 'through' notch classification, 22 rib clip hole samples were used where 11 contained 'through' notches. For 'corner' notch classification, 60 rib clip hole samples were used where 16 contained 'corner notches (8 right and 8 left). Four different corner notch sizes were explored: $0.03'' \times 0.03''$, $0.05'' \times 0.05''$, $0.07'' \times 0.07''$, and $0.10'' \times 0.10''$. The 11 parameters for the classification algorithm are given in Table 7.1. Details concerning the parameter constraints and binary encoding for genetic algorithm optimization are presented in Appendix C.

The fitness function to be minimized was developed using a combination of two classification algorithm performance measures. First, the relative operating characteristic was examined such that the threshold level to minimize the sum of the total percent

missed flaws and the total percent false calls was determined. Using the optimal threshold setting, a minimum value for the sum of missed flaws and false calls,

$$F_1(X,T_{min}) = \text{Missed Flaws (\%)} + \text{False Calls (\%)}, \tag{7.27}$$

was used as the first component of the fittness measure. For this study, equal weighting was given to missed flaws and false calls. For parameter settings that result in no missed flaws and no false calls, the first component of the fittness measure will equal zero. As a refinement to parameter optimization, a second component of the fittness measure is proposed based on the 'degree of statistical separation' between the two data sets (no-notch and notch sets.) Assuming normal distributions, the degree of separation can be represented by the following relation,

$$F_2(X) = | \mu_{flaw} - \mu_{no\ flaw} | / (\sigma_{flaw} + \sigma_{no\ flaw}). \tag{7.28}$$

This measure can be used to calculate the probability of a correct classification for the parameter setting through the following formula,

$$\text{Prob(correct classification)} = \Phi(F_2(X)), \tag{7.29}$$

where $\Phi(x)$ is the standard normal distribution function. Finally, the complete fitness measure can be represented by the following relation,

$$F(X,T_{min}) = \alpha_1 \cdot F_1(X,T_{min}) + \alpha_2 / F_2(X). \tag{7.30}$$

The weighting factors, α_1 and α_2, were set to 1.0 and 0.05 respectively. The genetic algorithm minimization routine used for this study was adapted from a routine written in Matlab [85]. The parameters for the genetic algorithm are presented in Appendix C.

Separate optimization results are presented in Table 7.2 for the 'through' notch, left 'corner' notch, and right 'corner' notch cases. For 'through' notch detection, correct classification of all 22 rib clip holes was achieved through the parameter optimization. For the combined 'corner' notch results, 14 of the 16 corner notches were properly classified with a 5.8 % false call rate. By eliminating the four 0.03'' × 0.03'' corner notch samples from the optimization problem, all 12 of the corner notch samples were classified with only a 1.9 % false call rate. The single false call rib clip hole did contain a bottom flaw. Due to the difficulty of this inspection problem, the performance of the optimization routine incorporating genetic algorithms is considered a success.

In addition to optimization of the inspection algorithm parameters, the optimization results can be used to better understand key features of the inspection problem. As an example, the optimal spatial location for the pulse-echo measurement is further from the specular hole reference than the optimal spatial location for the pitch-catch measurement. This optimization result corresponds well with the observations made from the parameteric simulated studies for transducer position presented in Section 7.7. Clearly, by locating the pulse-echo measurement further from the specular reference, measurement noise from sidewall signals is minimized.

Table 7.1. Optimization parameters.

X(1)	time gate start (from SPE reference) for pitch-catch data (CPC)
X(2)	time gate width for pitch-catch data (CPC)
X(3)	time gate start (from SPE reference) for pulse-echo data (CPE)
X(4)	time gate width for pulse-echo data (CPE)
X(5)	time/spatial adjustment for every 0.020" incremental spatial step
X(6)	spatial X gate start (from SPE reference) for pitch-catch data (CPC)
X(7)	spatial X gate width for pitch-catch data (CPC)
X(8)	spatial X gate start (from SPE reference) for pulse-echo data (CPE)
X(9)	spatial X gate width for pulse-echo data (CPE)
X(10)	spatial Y gate start (within range of 10 maximum scan length)
X(11)	spatial Y gate end (within range of 10 maximum scan length)

Table 7.2. Optimization results.

		'Through' Notch	Left Corner Notch	Right Corner Notch
X(1)	Time gate start CPC	*400*	360	360
X(2)	Time gate width CPC	*75*	200	200
X(3)	Time gate start CPE	*280*	220	240
X(4)	Time gate width CPE	*75*	175	125
X(5)	Time/spatial adjust for every 0.020" step	*22*	19	21
X(6)	Spatial X gate start CPC	*1*	9	6
X(7)	Spatial X gate width CPC	*4*	2	2
X(8)	Spatial X gate start CPE	*12*	13	11
X(9)	Spatial X gate width CPE	*4*	**2**	2
X(10)	Spatial Y gate start both	*3*	2	**7**
X(11)	Spatial Y gate end both	*8*	4	9
	Threshold Setting	**0.660**	**0.532 (0.532)**	**0.524 (0.401)**
	Percent Missed Flaws	**0.0 %**	**0.0 % *(0.0%)***	**0.0 % *(0.0%)***
	Percent False Calls	**0.0 %**	**0.0 % *(0.0%)***	**1.9 % *(5.8%)***
	Measure of Probability of Correct Classification (assume normal distribution)	**1.844**	**2.114 *(2.113)***	**1.748 *(1.342)***

( ) – results when four 0.03'' × 0.03'' corner notch samples were ***included*** in data set.